Journal of Materials Processing Tech. 323 (2024) 118229

Contents lists available at ScienceDirect

Journal of Materials Processing Tech.

journal homepage: www.elsevier.com/locate/jmatprotec

Synergistic effects of heat treatments and severe shot peening on residual stresses and microstructure in 316L stainless steel produced by laser powder bed fusion

Tejas Gundgire [a,*], Suvi Santa-aho [a], Timo Rautio [b], Antti Järvenpää [b], Minnamari Vippola [a]

[a] Tampere University, Materials Science and Environmental Engineering, P.O 589, 33100 Tampere, Finland
[b] Kerttu Saalasti Institute, University of Oulu, Pajatie 5, 85500 Nivala, Finland

ARTICLE INFO

Associate Editor: Marion Merklein

Keywords:
Additive manufacturing
Laser powder bed fusion
Stainless steel 316L
Residual stresses
Heat treatment
Severe shot peening

ABSTRACT

This study investigated the post-processing of laser powder bed fusion (LPBF) built 316L stainless steel components to address quality-related issues such as dangerous residual stresses and poor surface finish. Two different heat treatments (HT) at 600 °C and 900 °C, followed by severe shot peening (SSP), were employed to mitigate these concerns. The impact on roughness, residual stresses, microhardness, and microstructure in both as-printed and post-processed states was examined. Results indicate that the 600 °C HT fails to relieve residual stresses, while the 900 °C HT significantly reduces them by 90%. Furthermore, the SSP effectively reduced surface roughness by more than half of the initial values. The initial microstructures and residual stresses of the as-printed, 600 °C HT, and 900 °C HT samples differ, leading to distinct responses to identical SSP treatments. Notably, the 900 °C HT sample exhibited the deepest grain refinement after SSP and experienced the most substantial increase in surface hardness compared to the other samples. This research addressed critical quality issues in LPBF-built components by combining specific heat treatments and SSP. The 900°HT combined with SSP stood out as an effective method for relieving residual stresses and enhancing material properties. The distinct responses of the samples to post-processing highlight the importance of tailored treatments for LPBF components. These findings have significant implications for improving the quality and performance of LPBF components, with potential applications demanding improved fatigue and stress corrosion cracking performance.

1. Introduction

Additive manufacturing (AM) is a cutting edge manufacturing method thanks to its ability to print intricate near net shaped geometries (Attaran, 2017). AM has moved beyond the peak of the hype curve and is progressively evolving into an established manufacturing methodology (Ford and Despeisse, 2016). Powder bed fusion processes are popular for printing metallic components, especially in aerospace, nuclear and medical sectors (Song et al., 2011). A laser-based powder bed fusion (LPBF) also known as selective laser melting is a promising method and has been widely accepted in academia as well as industries for manufacturing components. Among several alloys that can be printed by LPBF, 316 L stainless steel is appealing due to its remarkable properties. With excellent properties such as outstanding corrosion resistance, biocompatibility, and high strength, 316 L finds its applications in range of industries including the nuclear and ship building industry (Bartolomeu et al., 2017).

Commonly, LPBF built 316L stainless steel is characterized by quality related issues in as printed condition such as poor surface finish, presence of detrimental residual stresses, etc (Gundgire et al., 2022). Lower process temperature and high thermal gradient during LPBF processing lead to complex heating and cooling cycles thereby inducing detrimental residual stress fields (Li et al., 2018). Expansion and contraction during melting and subsequent cooling of a layer are restricted by the underlying layer thereby inducing compressive and tensile residual stresses respectively (Mercelis and Kruth, 2006). Ulbricht et al. (2020) reported that detrimental tensile residual stresses were mainly present in the surface areas and bulk mainly consisted of compressive residual stresses. In addition to residual stresses, poor surface finish is also a major quality related challenge. The poor quality of surface in LPBF is mainly due to overlapping of melt pools and partially melted particles adhered to the surface. However, the surface roughness values at the micrometer level

* Corresponding author.
E-mail address: tejas.gundgire@tuni.fi (T. Gundgire).

https://doi.org/10.1016/j.jmatprotec.2023.118229
Received 6 October 2023; Received in revised form 9 November 2023; Accepted 22 November 2023
Available online 23 November 2023

were reported to be majorly dependent on partially melted powder particles rather than melt pool overlaps by Cabanettes et al. (2018). Furthermore, previous study by Beretta and Romano (2017) reported concentration of defects mainly in near surface areas. Dryepondt et al. (2021) reported the presence of a few large defects close to the sample surface and attributed it to the contour hatch overlapping. Yadollahi and Shamsaei (2017) also reported the presence of large voids along periphery of LPBF built Alloy 718 and attributed it to thermal effects between the powder bed and sample surface. Nafar Dastgerdi et al. (2022) reported that the surface and subsurface defects were more harmful to fatigue life than internal ones in direct metal laser sintered 316L. Amalgamation of all the above mentioned issues makes the surface and subsurface highly susceptible to premature fatigue or stress corrosion cracking failure. Therefore there is a strong necessity to address these quality related issues with post processing.

Usually, a stress relief HT is used to alleviate the detrimental tensile residual stresses. Chao et al. (2021) reported a stress relief of 24% from a HT at 400 °C for 4 h and 63% from a HT at 650 °C for 2 h. Moreover, Kong et al. (2018) referred a HT at 650 °C for 30 min as a stress relief HT. On the contrary, Gel'atko et al. (2023) reported presence of significant surface tensile residual stresses at the sample surface when subjected to stress relief at 650 °C for 4 h. Furthermore, Gundgire et al. (2022) reported that the magnitude of these tensile residual stresses was much higher at certain depth from the surface. These findings highlight need of studying residual stresses in detail along the depth in addition to surface measurements. Tensile residual stresses have consistently posed challenges in applications where fatigue and stress corrosion cracking are common as highlighted in previous studies by Rautio et al. (2022) and Toribio (1998). Their presence in surface and subsurface regions can be even more hazardous, potentially leading to premature failure. Therefore, relieving most of these detrimental residual stresses is a priority for such applications. Hamada et al. (2023) reported a stress relief of more than 80% at the surface and interior from a 30-minute heat treatment at 900 °C. This significant stress relief was reported to be beneficial for the fatigue property enhancement. A similar observation was made by Lai et al. (2021) for polished LPBF 316L stainless steel where a stress relief heat treatment at 900 °C for 2 h was proved beneficial for the improvement in fatigue properties, despite a slight reduction in hardness values following the stress relief process. Apart from residual stresses, these HTs also affect the microstructure of as printed specimens. Salman et al. (2019) reported coarsening of the cellular microstructure with an increase in the HT temperature. Shin et al. (2021) reported the dissolution of cellular microstructure along with decreased dislocation density after 1100 °C HT which resulted in reduction of hardness and tensile strength and increase in elongation. Furthermore, Yin et al. (2021) and Zhang et al. (2022) investigated the different HT protocols and their subsequent effect on microstructure as well as mechanical properties.

Additionally, post stress relief, to further induce compressive residual stresses and to modify the near surface area microstructure, post processing methods such as shot peening or laser shock peening can be applied (Bagherifard et al., 2016). A promising method namely severe shot peening (SSP) can be applied to induce beneficial compressive residual stresses along with several other advantageous surface modifications (Liu et al., 2020). It is an intensive shot peening protocol that uses either higher kinetic energy or increased exposure time of shot peening media to achieve the surface and subsurface modifications. SSP is usually known to degrade surface quality in rather smooth conventionally manufactured steels due to indentations formed by bombardment of shot peening media. However, in LPBF and generally in AM built components because the surface is already rough, method like severe shot peening could even out the irregularities on the surface resulting in better surface finish than as printed state. Previous studies by Gundgire et al. (2022) and Rautio et al. (2020) on SSPed LPBF 316L stainless steel reported a significant reduction in roughness values along with beneficial improvements such as induction of increased and more profound compressive residual stresses, enhanced grain refinement, etc.

The majority of the literature is concentrated on investigating the effect of HT on microstructure, mechanical as well as wear and corrosion behaviours. These heat treatments at different temperatures result in distinct microstructural changes. Since the crucial surface areas are highly susceptible to failure crack initiation there is a strong requirement for further surface enhancement to boost its resistance to failure. A method like SSP if applied could have diverse outcomes depending on the starting microstructure after HT. To the best of authors' knowledge, the combined post processing protocol integrating various heat treatments with a severe shot peening for LPBF built 316L stainless steel is not comprehensively investigated in the existing literature. This fuelled investigations in the present study in which as printed LPBF 316L stainless steel specimens were subjected to heat treatments at two different temperatures followed by an identical SSP protocol by Almen intensity of 358 A. The samples in as printed, heat treated and severe shot peened states were studied in detail for microstructure, roughness, grain deformation, residual stresses, and microhardness. It is worthwhile to mention that the SSP term is not explicit and therefore needs to be described quantitatively. SSP in authors previous work referred to the Almen intensity of 240 A (Gundgire et al., 2022). However, SSP term in present work refers to the a greater Almen intensity of 358 A to obtain the highest possible surface and subsurface modifications. The higher Almen intensity of 358 A was achieved by increasing peening exposure time during the process.

2. Material and methods

2.1. LPBF built 316L stainless steel and post treatment

The powder used in this study had a spherical form and had particle diameters between 20 and 53 μm. Table 1 presents the chemical constituents of the used powder. The samples with a size of 80 × 20 × 2 mm were manufactured in SLM solution's SLM 280HL machine situated at Future Manufacturing Technologies, Nivala, Finland. The specimens were printed in vertical orientation i.e. perpendicular to the base plate along the sample length of 80 mm (refer Fig. 1). Machine supplier's recommended standard printing parameters were used to print the samples. Throughout the entire printing process, the printing cabinet was maintained at 100 °C. The laser utilized was 200 W and had a Gaussian laser profile with a spot diameter of 0.1 mm. The hatch spacing was set to 0.12 mm. Furthermore, the printing settings involved 800 mm/s scanning speed and 30 μm layer thickness. All the samples were detached from the base plate for further post processing as well as investigation.

An Argon-filled muffle furnace (Sarlin 1000HS-436) was utilized for the stress relief HT. The HT was conducted at two distinct temperatures, 600 °C and 900 °C for 2 h and 0.5 h, respectively. The objective behind opting for a 900 °C HT for 0.5 h was to achieve maximum stress relief along with an aim to achieve the dissolution of cellular microstructure which was inspired by authors recent work (Hamada et al., 2023). Overall, the aim was to have as printed, 600HT (2 h), and 900HT (0.5 h) samples which have some differences in stress levels, hardness, and microstructure. This was to be followed by an identical SSP protocol and investigate its response to these different sample conditions.

Severe shot peening using an air blast system was carried out within an enclosed cabinet. During this operation, an industrial robot, a nozzle, and a shot blasting pot were utilized. The selected shot media was a martensitic chromium media (STELUXC C60), which had a size range of 0.7–1.2 mm and a hardness of 42 HRC. The peening process was

Table 1
The chemical constituents of 316 L powder utilized in this study.

Element	Fe	Cr	Ni	Mo	Mn	Si	C	O
wt%	bal.	17.0	12.5	2.5	1.6	0.8	0.009	0.051

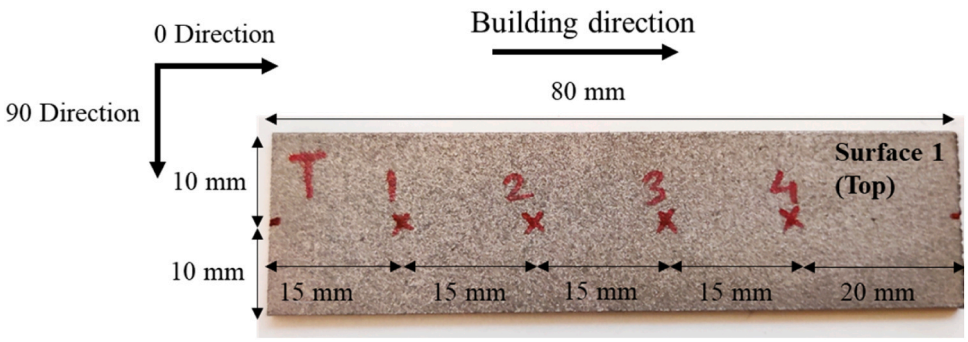

Fig. 1. Measurement strategy for residual stresses.

conducted at a nozzle distance of 70 mm and a pressure of 7.4 bar. The nozzle velocity was 50 mm/s. Utilizing type A strips, the Almen intensity measurement yielded a saturation intensity of 358 A. The shot peening coverage ratio approached nearly 100%. A comprehensive account of the shot peening experiments can be found in the authors previously published work (Gundgire et al., 2022; Rautio et al., 2022). Samples in three different states i.e., as printed, heat treated at 600 °C and heat treated at 900 °C were subjected to severe shot peening on both sides i.e. surface 1 and surface 2 (refer Fig. 1) by Almen intensity of 358 A. In author's previous work, Almen intensity of 240 A was used for SSP. In the present study, the Almen intensity of 358 A was used to achieve a profound effect. The various sample states studied in this work are listed in Table 2 along with their designations which will be used hereafter in the text.

2.2. Microstructural characterization

To study the effect of HT through microscopy, the samples were prepared by sectioning them in two different orientations: parallel and perpendicular to the direction of the building. These samples were then embedded in a conductive resin. For topographic investigation, the specimens were sliced and then ultrasonically rinsed in ethanol. Specimens were sliced alongside the cross section and were embedded in a conducting resin for the cross sectional investigation. The mounted samples underwent grinding using 320–2000 SiC papers. Subsequently, the ground specimens were subjected to a diamond suspension polishing (particle sizes: 3 μm and 1 μm) using a Tegramin 30 (Struers, Denmark) semi-automatic polishing machine. A V2A etchant was utilized for etching which is a solution of 10 parts water to 10 parts hydrochloric acid to 1 part nitric acid. The etchant was heated until fumes became visible, and then the sample was immersed in it for a duration of 8–12 s

A scanning electron microscope (ULTRAplus, Zeiss, Germany) was utilized for all of microstructural investigation. The cell size of the specimens was determined with the line intercept method. For electron backscatter diffraction (EBSD) samples, an extra polishing step with 0.05 μm colloidal silica suspension was carried out in addition to the previously mentioned protocol. For EBSD analysis, a system by Oxford Instruments (United Kingdom) coupled with a scanning electron microscope was used. A large area of 1100 × 850 μm was scanned with 1 μm steps to anticipate the microstructure after HT. Fine scans measuring 200 × 50 μm were conducted with a step size of 94 nm to examine the impact of SSP. Data collection was done using the Aztec software and the data was processed in the Aztec crystal software for inverse pole figure (IPF) maps. 3D optical profilometry was used to capture 3D topographic images and for measurement of surface roughness. A 10x objective magnification was utilized on a 3D optical profilometer (Alicona InfiniteFocus, G5, Austria) to scan a 5 mm × 5 mm area. A zigzag line spanning over 50 μm was drawn over the scanned areas to calculate the average roughness values (Ra).

Table 2
Sample states along with their designations.

Designation	Sample state
AB	As printed
600HT	Heat treated at 600 °C, 2 h
900HT	Heat treated at 900 °C, 0.5 h
AB+SSP	As printed followed by severe shot peening
600HT+SSP	Heat treated at 600 °C (2 h) followed by severe shot peening
900HT+SSP	Heat treated at 900 °C (0.5 h) followed by severe shot peening

2.3. Residual stress measurements

The measurement of residual stresses was conducted using a Xstress 3000 equipment (Stresstech Oy, Finland). It is an X-ray diffraction (XRD) based diffractometer which utilizes the modified chi method for the residual stress measurements. MnKα radiation source with a diffraction angle of 152.3° was deployed on 311 lattice plane with a 3 mm collimator. The Young's modulus of 184 GPa along with Poison's ratio of 0.28 was used for the measurements. More details on the equipment and measurement principle are availabe in author's earlier research (Gundgire et al., 2022). It is important to note that all the residual stress measurements were performed after removing samples from the base plate. The residual stress measurements on the surface were conducted on the same specimens before and after the post processing to achieve comparable results. For each sample, surface residual stresses were measured at 4 different locations in the building direction (0 direction) and the direction orthogonal to it (90 direction) as shown in Fig. 1. A similar measurement strategy was used to measure the surface RS on both surfaces i.e., surface 1 (top) and surface 2 (bottom). The measurement of residual stresses along the depth was performed on all the samples at location 3 from surface 1 and surface 2. A MoviPol-5 electrolytical polisher (Struers, Denmark) was utilized for material removal during the measurements. A dial gauge (Mitutoyo, Japan) was utilized to monitor the material's removal depth. A2 electrolyte comprised of ethanol and perchloric acid was used. More information about the depth profile measurement method can be obtained from authors' earlier research (Gundgire et al., 2022; Santa-Aho et al., 2021).

2.4. Microhardness measurements

MMT-X7 (Matsuzawa, Japan) equipment with a 0.05 Kg load was used for microhardness measurements. Measurements were conducted across sample the cross section, commencing 25 μm below the surface to anticipate effect of SSP. The distance between each measurement was 50 μm along the depth. The procedure was replicated 3 times for each sample. Furthermore, the average microhardness of as printed and heat-treated samples was calculated from 10 separate measurements along the cross section.

3. Results

The as printed specimens were exposed to two distinct HT temperatures i.e. 600 °C and 900 °C. Subsequently, the as-printed and HT samples underwent a severe shot peening protocol. All these samples were studied in as printed as well as post processed conditions for residual stresses, microstructure, surface roughness, grain refinement as well as microhardness. The studied results are reported and deliberated systematically in this section.

3.1. Effect of heat treatment on microstructure

The microstructure of AB, 600HT and 900HT along the building direction and perpendicular to it is shown in Fig. 2a-c and a′-c′ respectively. As printed specimen showed a typical microstructure which includes columnar grains running across the building direction, half cylindrical melt pools and sub-grained cellular microstructure as shown in Fig. 2(a-a′). The 600 °C stress relief HT did not alter the microstructural state from the as-built condition. However, after the 900 °C HT, substantial changes in the microstructure were observed. The clearly seen melt pool boundaries in as printed and 600 ° HT samples seemed to be fainted indicating almost dissolution of the melt pool based microstructure. Also, the contrast due to segregation of Mo and Cr which can be seen from as printed and 600 °C HT is not seen any more in the 900°HT sample. At higher HT temperatures atomic diffusion takes place which results in dissolution of the melt pool based microstructure (Elangeswaran et al., 2022). Even though there are significant microstructural changes, the columnar grain structure is maintained after 900 °C HT which can be seen from Fig. 2(c′). Grain coarsening in the 900HT sample is not visually evident in Fig. 2(c′) which aligns with a previous investigation by Ronneberg et al. (2020) that reported resilience to grain coarsening at 1040 °C HT.

High magnification micrographs in as printed, 600 °C HT and 900 °C HT are shown in Fig. 3(a-c). The typical sub-grained cellular microstructure in as printed condition can be seen in Fig. 3(a). These cells can be easily resolved with their bright boundary contrast under electron microscopy (Saeidi et al., 2015). This bright contrast indicates the higher composition of Mo and Cr at the cell boundaries (Wang et al., 2018). The average size of the cell was evaluated by using the line intercept method and calculated to be 491 ± 8 nm for as printed sample. The cellular microstructure was maintained after 600 °C HT along with the bright contrast. However, the average cell size was increased to 639 ± 7 nm as depicted in Fig. 3(d). Salman et al. (2019) also observed growth of the cell size with increasing heat treatment temperatures. This could be attributed to the slight diffusion of chemical segregations at cell boundaries. The cellular structure was almost dissolved after 900 °C HT which is evident from Fig. 3(c). Also, the bright contrast at cell boundaries was not visible anymore indicating dissolution of Mo and Cr in the

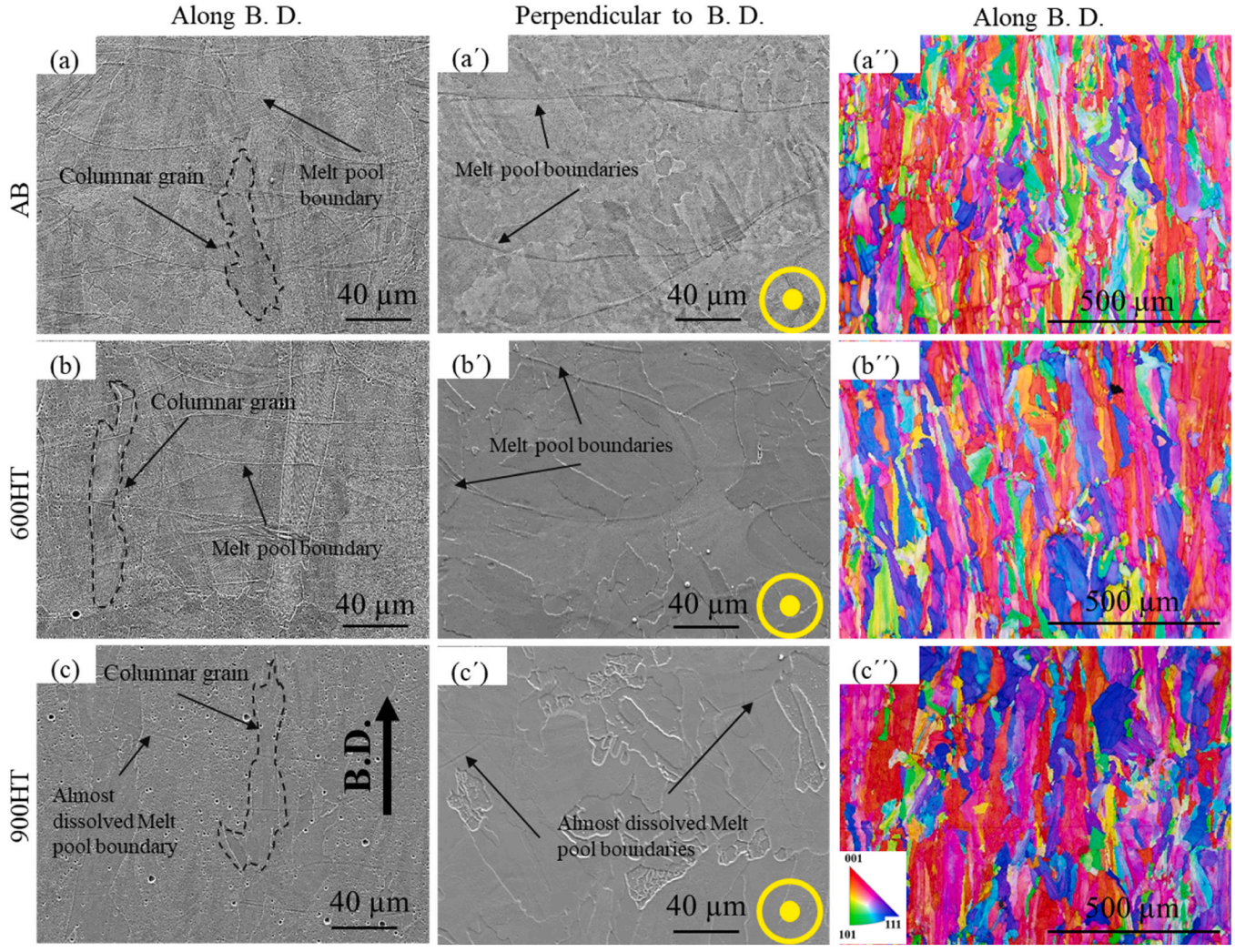

Fig. 2. SEM micrographs of the AB, 600HT and 900HT specimens a-c) along the building direction, a′-c′) perpendicular to the building direction. a-c′) EBSD maps of the AB, 600HT and 900HT specimens along the building direction.

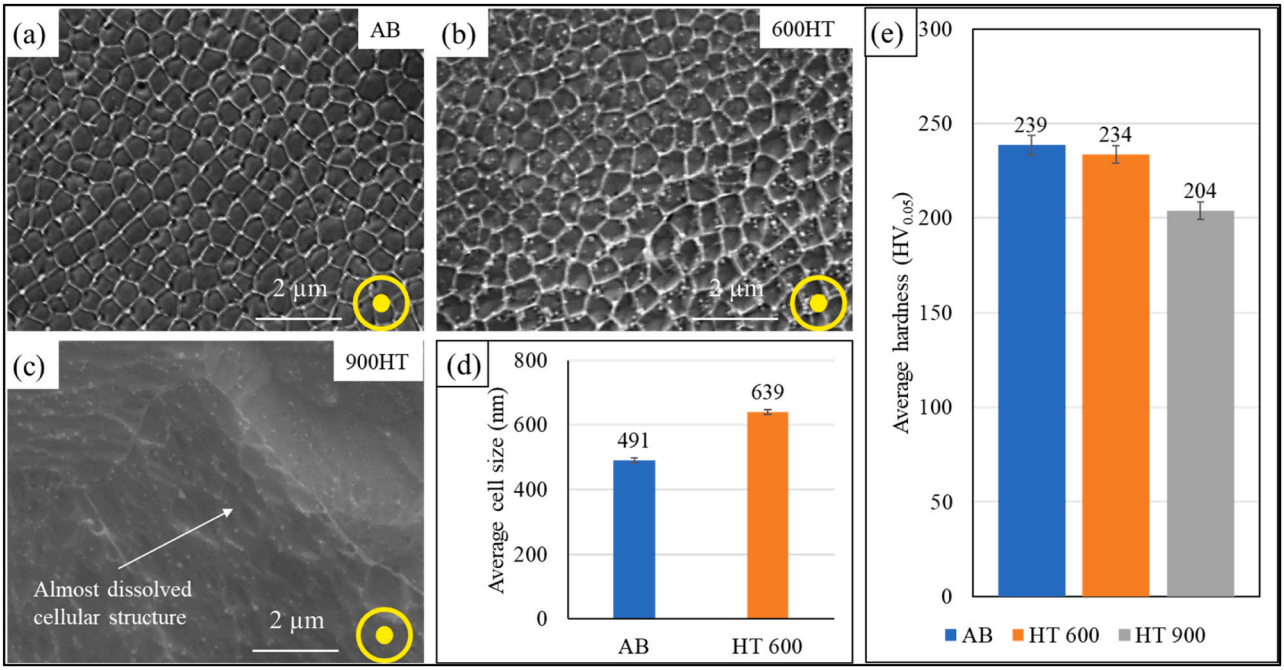

Fig. 3. (a, b,c) High magnification micrographs perpendicular to the building direction showing cellular microstructure in as printed, 600HT, and 900HT samples respectively, (d) average cell size and (e) microhardness values.

matrix. As mentioned earlier cell boundaries are chemical segregations, hence they are prone to diffusion at higher HT temperatures (Ronneberg et al., 2020). The HT at 900 °C could have led to significant diffusion and thereby the dissolution of cellular microstructure.

The evolution of cellular microstructure due to heat treatments also had an effect on hardness of the samples. The average microhardness values shown in Fig. 3(e) were averaged from ten measurements. As printed sample had an average microhardness of 239 ± 5 HV. Hardness in as printed condition is governed by several parameters during processing such as scan velocity (Lin et al., 2019), orientation as well as layer thickness (Saxena et al., 2021). It was slightly reduced after 600 °C HT to a value of 234 ± 4 HV which could be correlated to increased cell size. The microhardness value dropped to a value of 204 ± 4 HV after 900 °C HT which can be linked to the dissolution of the cellular microstructure. These findings are aligned with previous studies by Kamariah et al. (2017) and Shin et al. (2021) which also reported a drop in hardness values with rise in HT temperatures.

3.2. *Effect of HT+SSP*

3.2.1. *Topography and cross section*

Micrographs depicting sample surface and cross-sections are shown in Fig. 4. As printed sample had the presence of ball-like particles present on the surface which can be seen in Fig. 4a). It was described as balling effect in previous findings by Li et al. (2012). It constitutes of partially melted granules of powder clung to the surface. Sendino et al. (2023) reported that majority of the adhered particles were the smallest sized particles from the powder batch citing a higher tendency of smaller particles for partial melting compared to the larger ones. A layered structure due to the solidification of melt pools is also evident from the same figure. The cross-sectional micrograph (Fig. 4(a)) also indicated uneven surface of the as printed samples. The presence of layered structure even after the 600 °C, 2 h HT (refer Fig. 4(b-b)) implies that it did not alter topography as well as cross-sectional morphology from the as printed condition. On the contrary, a topographic micrograph after 900 °C HT does not show any layered structures indicating its dissolution. It is worthwhile to mention that visually more number of ball like particles were seen on the 900HT sample when compared to the as printed and 600HT samples. The exact reason is not clear; however, it could be due to a combination of various factors such as dissolution of layered melt pool structure, residual stress relief (presented later in the text) as well as loosening of particles on the surface. The combined effect of above-mentioned factors could have led to release of some of the half-melted powder particles which could have led to their dense appearance on the surface. Similar speculations were previously made by Cabanettes et al. (2018) after HT of LPBF built Ti–6Al–4 V.

SSP by Almen intensity of 358 A resulted in evening out of the surface irrespective of the starting balling effect which can be seen from both the topographic as well as cross-sectional micrographs shown in Fig. 4(d-d̀), (e-è) and (f-f). The cross-sectional micrographs show deformation in the top surface layers. They appear faint in the micrographs as it is difficult to reveal them with etching because of nanometre sized grains in that zone. The EBSD chapter later in the text discusses the same in detail. Ball like powder particles were entirely evened out on the surface after SSP. Also, indentation overlaps were formed on the sample surfaces due to intense pounding of the peening media as pointed out in Fig. 4(d). These indentation overlaps seemed to be increasing from as printed to 600HT to 900HT conditions after SSP. This could be attributed to the decreasing hardness values of heat-treated samples making the surface less resistant to deformations.

3.2.2. *Roughness*

3D topographic images of different samples obtained by an optical profilometer are shown in Fig. 5(a–f). The corresponding average surface roughness (Ra) values measured from the 3D topography are shown in Fig. 5(g). The as printed sample was quite rough and had a Ra value of 11.12 µm. The surface quality of as printed surface depends on a combination of a variety of process settings including scanning strategy (Kruth et al., 2008), laser power (Dursun et al., 2019), scanning speed (Lin et al., 2019) and layer thickness (Shi et al., 2020). While using optimal process parameters can reduce the extent of surface irregularities, complete elimination of these irregularities is not achievable. Surface roughness value of as printed sample is mainly affected by two entities. First is overlapping half cylindrical melt pools and second is partially melted particles on the surface. Previously, Greitemeier et al. (2016) and Panov et al. (2022) reported that partially melted particles

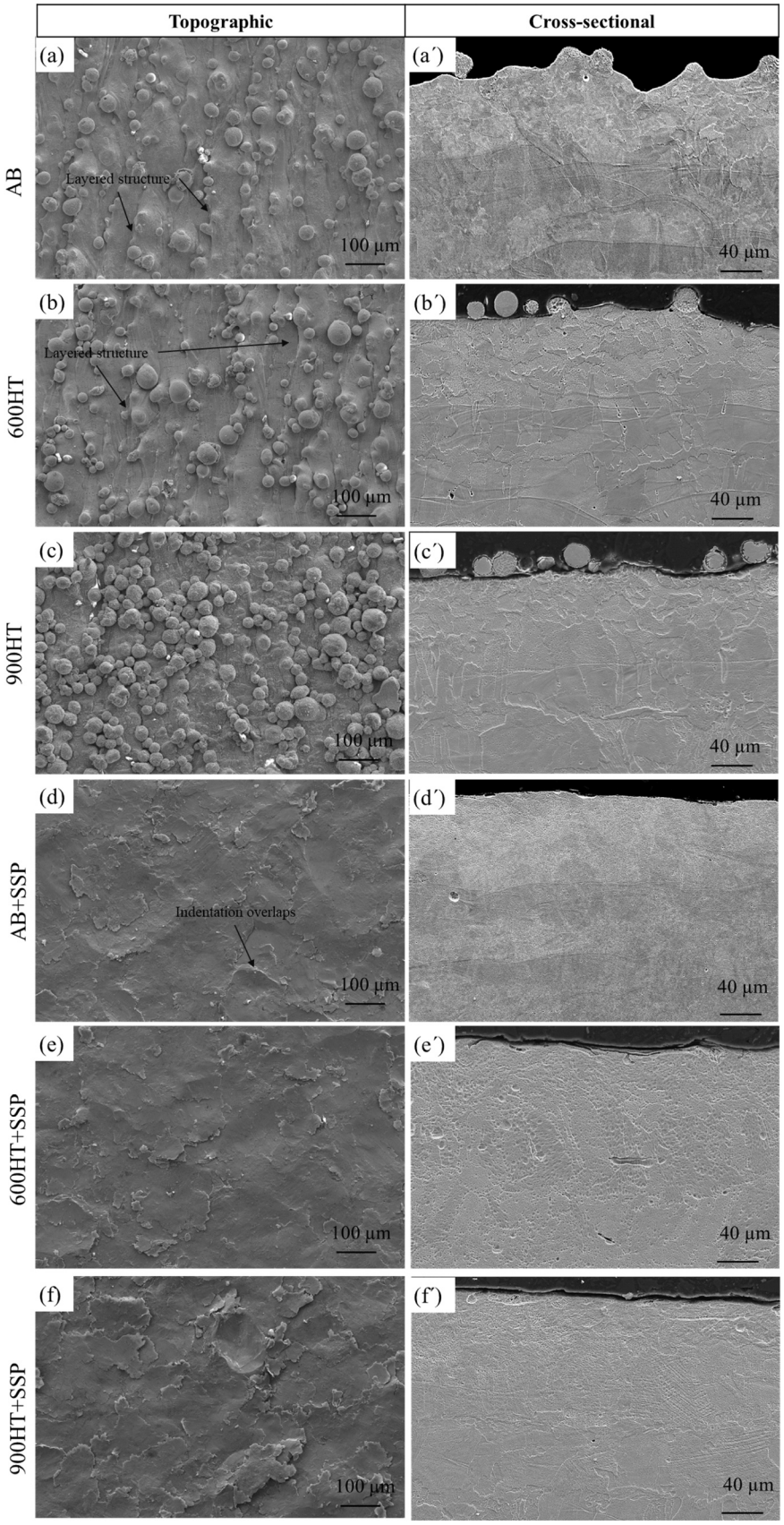

Fig. 4. Micrographs depicting sample surface and cross-sections a-a) AB, b-b′) 600HT, c-c) 900HT, d-d) AB+SSP, e-e) 600HT+SSP and f-f) 900HT+SSP.

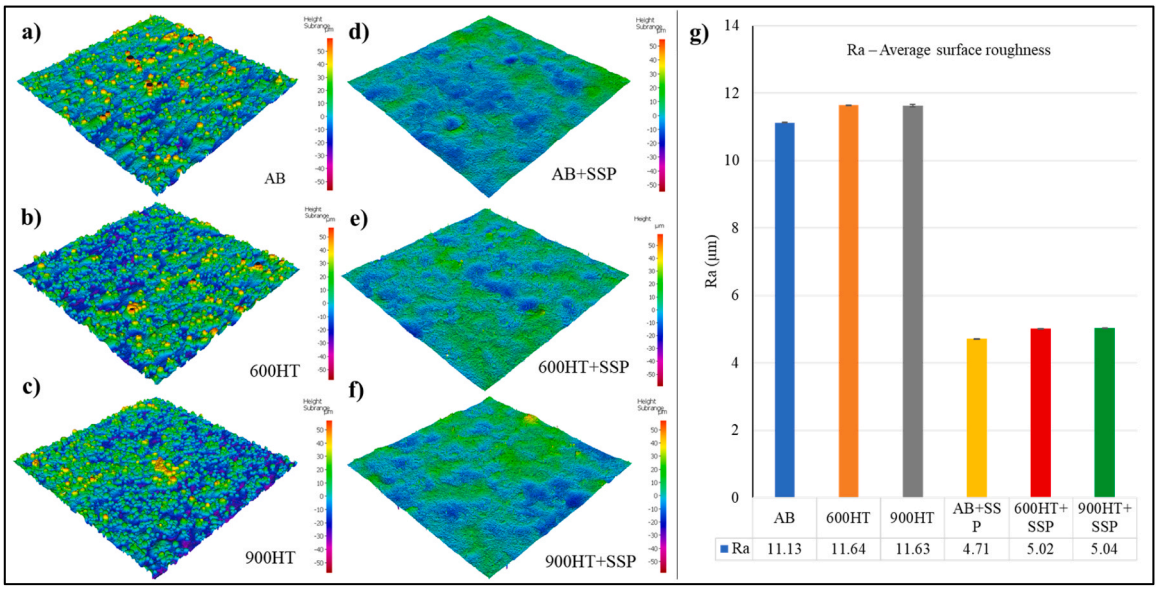

Fig. 5. a-f) 3D optical profilometry images and g) average surface roughness (Ra) values of the specimens.

mainly affect the roughness value while overlapping of melt pools had a negligible effect at micrometre level. Roughness induced due to overlapping of melt pools was termed as primary roughness while roughness induced due to partially melted powder particles was termed as secondary roughness. The surface appeared similar to that of as printed samples after HT at 600 °C and 900 °C with Ra values of 11.64 and 11.62 µm. As previously mentioned, the melt pool based microstructure was almost dissolved after the 900 °C HT. However, it did not have any effect on the Ra value which confirmed the negligible contribution of melt pool overlaps on the surface roughness values at micrometre level.

The as printed as well as heat treated samples exhibited high roughness values. Surface roughness has a negative effect on fatigue strength and therefore it is critical to either reduce or eradicate it (Nakatani et al., 2019). Subjecting the AM built samples to SSP has been proven beneficial for a significant reduction of roughness values thereby producing a much better surface (Gundgire et al., 2022). SSP by Almen intensity of 358 A levelled out the sample surface which can be seen from Fig. 5(d). These can be ascribed to the intense pounding of peening media smoothing out the sample surface. The partially melted powder particles are no longer visible on the surface. SSP reduced the Ra value of

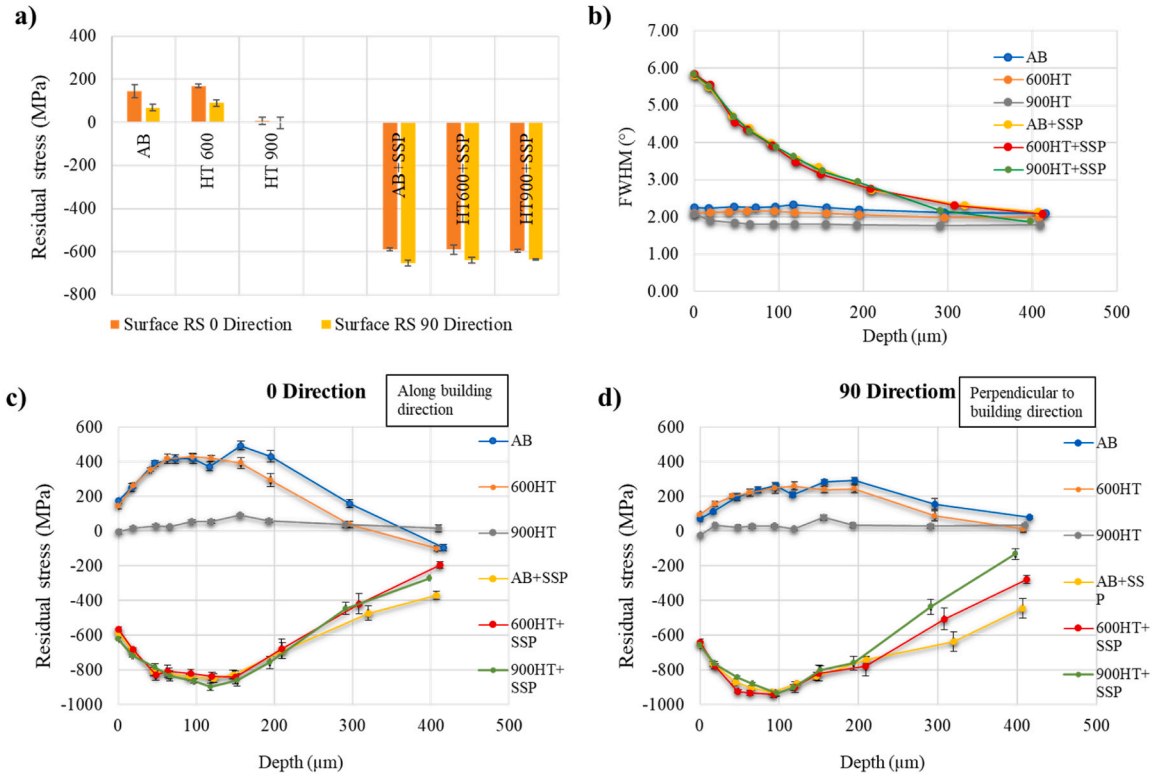

Fig. 6. a) Surface residual stresses, b) FWHM in relation to depth from surface, c) residual stress depth profiles along the building direction (0) and d) depth profiles perpendicular to the building direction (90).

as printed sample from 11.12 μm to 4.70 μm which is less than half of the original value. Similar results were obtained for the 600HT and 900HT samples with roughness values being reduced to 5.02 and 5.03 μm respectively.

3.2.3. Residual stresses

Surface residual stress values averaged from four measurements are shown in Fig. 6a). 0 measurement direction represents the building direction while 90 direction represents the direction perpendicular to it. It is worthwhile to mention that the surface residual stresses were also measured from surface 2 (refer to Fig. 1) and the values were similar to that of surface 1. Therefore, only values from surface 1 are reported in Fig. 6a) for the sake of brevity. The sample in its as-printed state exhibited surface residual stresses of 144 ± 31 MPa in the direction of the build and 68 ± 14 MPa perpendicular to it. The high thermal gradient values along building direction during sample manufacturing could have led to larger residual stresses in building direction. Similar observations were reported previously by Bian et al. (2018) and Yadroitsev and Yadroitsava (2015). Also, in the authors' previous work where the building direction was along width of the sample countered to the current study (Gundgire et al., 2022), residual stresses were larger along the width i.e. the building direction. The 600 °C, 2 h HT did not alleviate any of the residual stresses from as printed state. The measured values were 169 ± 8 MPa and 90 ± 15 MPa in the direction of the build and the direction perpendicular to it respectively. On the contrary, the 900 °C HT relieved more than 90% residual stresses from the as printed state. The measured values were 6 ± 17 MPa and − 2 ± 26 MPa along 0 and 90 direction respectively.

Severe shot peening by Almen intensity of 358 A induced large compressive residual stresses on sample surfaces irrespective of the starting residual stress values (Fig. 6(a)). Again, the measured values were similar on surface 2 as that of surface 1. Therefore, only surface 1 values are reported for brevity. For the AB+SSP sample, the measured values were −589 ± 7 MPa and −652 ± 13 MPa respectively in 0 and 90 directions. 600HT+SSP sample had residual stress values of −590 ± 22 MPa and −638 ± 14 MPa while 900HT+SSP sample had −596 ± 7 MPa and −636 ± 4 MPa along 0 and 90 directions, respectively. Even though residual stress values seem to have reached similar values after SSP, the starting values were different. Hence, the total change in residual stress values in the 0 direction is 734 MPa, 759 MPa and 603 MPa for as printed, 600HT and 900 HT samples. This shows that the change in residual stresses was much higher (22–25%) in as printed and 600HT samples when compared to the 900HT sample. This higher change in as printed and 600HT samples could be attributed to the already present pre-stressed state prior to the SSP. Previously, Zhan et al. (2012) reported that prestressing the samples before shot peening could result in achieving higher compressive residual stress values after shot peening. The mentioned pre-stressing behaviour was also seen in residual stresses along the 90 direction.

Residual stress depth profiles along cross section for all the samples in 0 and 90 directions are shown in Fig. 6c) and d) respectively. For as printed sample, residual stress values kept increasing along the depth and reached a peak value of 420 MPa at a depth of around 100 – 200 μm after which the values started decreasing and reached 0 MPa residual stress at a depth of 300–400 μm. After reaching the zero value the profile tends to shift in compressive residual stress zone. These observations are in line with observations made by previous studies by Bian et al. (2018) and Ulbricht et al. (2020). Maximum residual stress at a depth of 100 – 200 μm could be due to the overlapping of the shell core strategy thereby resulting the complex heating and cooling cycles. The 600HT sample also showed a similar depth profile as that of as printed one. On the contrary, since the surface residual stresses were almost relieved after 900 °C HT, the profile was relatively straight along the depth with a maximum value of 92 MPa at 140 – 170 μm depth. Also, the profile did not show any tendency to shift in compressive residual stress zone indicating relief of compressive residual stresses in the bulk. An analogous trend of depth profiles was observed along the 90 direction with the only difference being lower values of maximum tensile residual stresses. This makes sense as the surface residual stress values were much less in the 90 direction than in the 0 direction.

As mentioned earlier, SSP by Almen intensity of 358 A induced larger compressive residual stresses on the surface. Similar depth profile behaviour was observed for AB+SSP, 600HT+SSP and 900HT+SSP samples. The magnitude of compressive residual stresses along the 0 direction kept increasing along the depth and reached maximum values of more than −800 MPa at the depth ranging from 100 to 150 μm. The compressive residual stresses were above −600 MPa and −400 MPa at depths of 200 and 300 μm respectively from the surface in all the samples. After which the residual stress values tend to decrease towards 0 MPa as shown in Fig. 6(c). It is worthwhile to mention that the pre-stressing phenomenon mentioned earlier can also be related to depth profiles with the lowest change in residual stress values for the 900HT+SSP sample. Depth profiles along the 90 direction also exhibited similar behaviour as that of the 0 direction. Overall, the greater and advantageous compressive residual stresses were induced on the critical surface and subsurface areas which completely reversed the depth profile from as printed condition.

Fig. 6(b) displays the Full Width Half Maximum (FWHM) graph across the depth. It is important to note that the error bars were minimal, with a range of ± 0.06 to ±0.12. The as printed sample had an FWHM value of 2.26 on the surface and was maintained to a nearby value along the depth. 600HT samples had a value of 2.10 and maintained a similar profile as that of as printed one. The 900HT sample had an FWHM of 2.09 on surface but it kept decreasing along depth till FWHM value of 1.80 and then remained steady afterwards. SSP led to significant increase in the FWHM values at the surface for all three samples. The values near the surface reached in the range of 5.80–5.90 which is almost 3 times the base value. This could be ascribed to the surface hardening caused by intense bombardment of peening media. The FWHM values gradually diminished with depth until they reached their respective baseline levels at approximately 400 μm depth.

3.2.4. EBSD

Inverse pole figure (IPF) maps of as printed, heat treated and severely shot peened samples are shown in Fig. 7. The smallest possible step size of 94 nm for this particular area (50 ×200 μm) was used to resolve the maximum of the tiny, deformed grains. A previous report by Liu et al. (2020) suggested use of smaller step sizes reduces so called zero solutions thereby resulting in higher indexing. The undeformed surface of as printed sample can be evidently seen from Fig. 7(a). Heat treatments with 600 °C and 900 °C did not alter the surface condition which is evident from Fig. 7(b) and (c). Severe shot peening by Almen intensity of 358 A resulted in a grain refinement depth of 45–55 μm from the surface. This could be ascribed to the intense pounding of peening media inducing surface deformation. The deformed area had a visually gradient distribution of grains, with the smallest grains located closest to the surface, and their size progressively increased towards the depth. The 600HT+SSP sample also exhibited a grain refinement depth of ~ 45–55 μm which was similar to that of as printed one. On the contrary, the 900HT+SSP samples had a deeper grain refinement depth of ~ 80–90 μm. This could be attributed to the dissolution of cellular microstructure thereby reducing the hardness and offering lesser resistance to grain deformation. Overall, the depth of deformed grains that can be achieved with severe shot peening is dependent on the starting microstructure as well as hardness values before the treatment.

3.2.5. Microhardness

Microhardness values measured with a load of 0.05 kg along the depth of the samples are shown in Fig. 8. The first measurement was taken at 25 μm below the surface followed by a 50 μm gap between each of the next measurements. For brevity, only one of the three repeated hardness profiles per sample is shown on the plot, as all three profiles

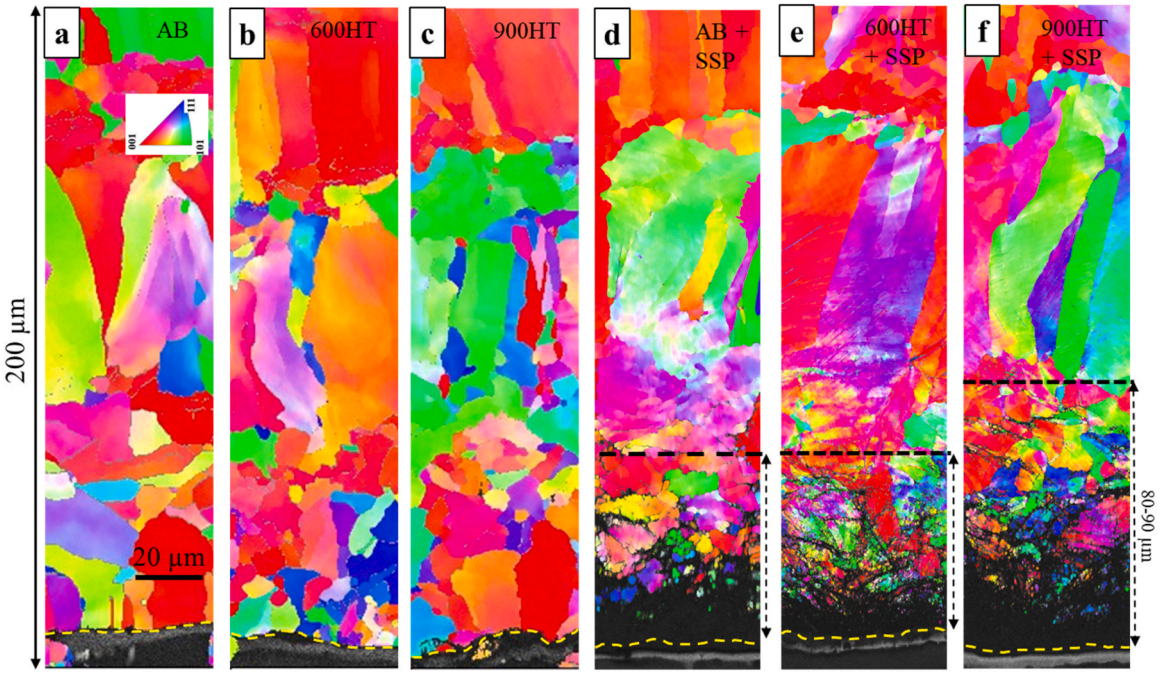

Fig. 7. Inverse pole figure (IPF) maps of samples, with the uppermost surface layer delineated by a yellow spaced line.

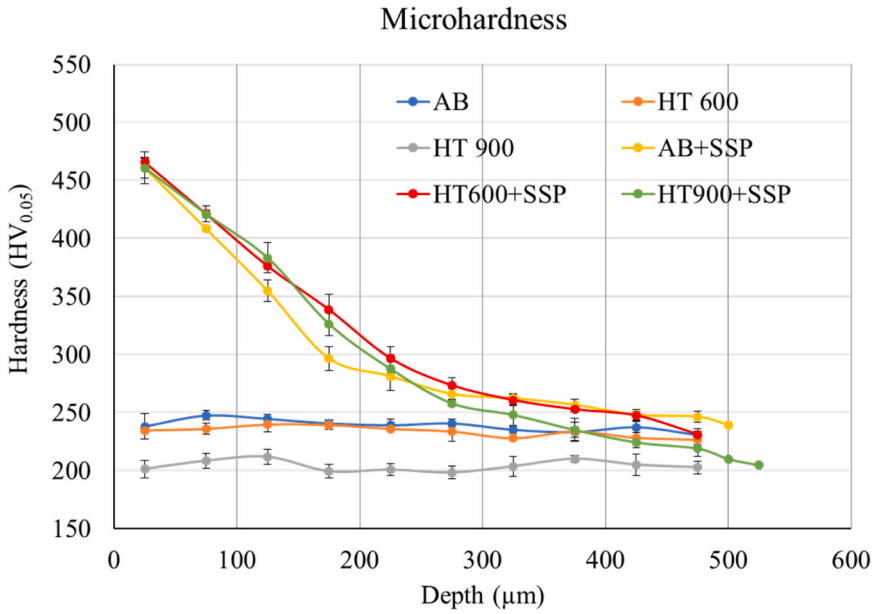

Fig. 8. Microhardness depth profile.

exhibited similar results. As mentioned earlier, the average hardness values of as printed, 600HT and 900HT samples were 239 ± 5 HV, 234 ± 4 HV and 204 ± 4 HV respectively. All these samples had similar values near the base material values along the depth profile which can be seen from the plot. The base values of as printed and 600HT samples were close to each other and therefore, they appear to be similar in the depth profile. On the contrary, the base value of 900HT was significantly lower compared to them which makes it easily resolvable in the plot.

Severe shot peening by Almen intensity of 358 A resulted in increased hardness in surface layers for as printed, 600HT and 900HT samples. Severe bombardment of peening media leads to work hardening and thereby increased hardness (Kumar et al., 2019). The hardened surface layer increases the mechanical properties at the surface thereby increasing the resistance to crack initiation (Rautio et al., 2022). The measured hardness below 25 µm of the surface was 461 ± 14, 466 ± 4 and 461 ± 8 for AB+SSP, 600HT+SSP and 900HT+SSP samples, respectively. This indicates remarkable surface hardness improvement irrespective of starting hardness values before SSP. As printed and 600HT samples had a 93% and 99% increase compared to the base values as depicted in Table 3. This can be ascribed to the work hardening and grain refinement caused by the bombardment of peening media. The 900HT samples on the other hand had the highest percentage increase of 126% compared to the base values. This also can be ascribed to the work hardening and grain refinement caused by the SSP. The hardness affected depth for the as printed and 600HT samples was approximately 300 – 400 µm while it was in the range of 475 – 525 µm for the 900HT

Table 3
Percentage change in microhardness values before and after severe shot peening.

Sample	Before SSP	After SSP (25 μm from surface)	% Increase from base values
AB	239	461	93%
HT 600	234	466	99%
HT 900	204	461	126%

sample. This could be attributed to relatively higher difference between peening media and sample surface hardness in 900HT sample compared to the other two. This difference could have led to deeper work hardening and thus the relatively higher hardness affected depth (Bagherifard et al., 2018).

4. Discussion

The interplay between the 900HT and SSP processes takes centre stage in the present study, with remarkable findings that underscore their combined impact on material and surface properties. These two techniques, when used in conjunction, bring about substantial transformations in the material's microstructure, residual stresses, and other surface characteristics. This combination's remarkable performance commenced with a substantial mitigation of initial surface residual stresses after 900HT, attaining an extraordinary reduction exceeding 90%. The initial stress levels of 144 ± 31 MPa in the building direction and 68 ± 14 MPa perpendicular to the building direction were significantly diminished to 6 ± 17 MPa and − 2 ± 26 MPa, respectively. The reduction in residual stresses achieved through this heat treatment was a result of the thermal relaxation of internal stresses within the material, an essential mechanism that forms the basis of stress relief by heat treatment. This showcases the impressive capability of the high-temperature HT to alleviate residual stresses. Furthermore, the reduction in hardness after 900HT to 204 ± 4 HV from 239 ± 5 HV in as printed condition as indicated in Fig. 3(e), may suggest a potential decrease in tensile behaviour. However, for applications where fatigue and stress corrosion cracking are pivotal concerns, the presence of tensile residual stresses, particularly in the surface and subsurface regions, poses significant challenges. Therefore, the priority lies in mitigating these detrimental tensile residual stresses, even if it comes at the expense of some reduction in hardness and tensile behaviour. This approach aligns with findings in the literature, as evidenced by a report from Lai et al. (2021). It is worth noting that even with a slight reduction, the hardness exhibited by the 900HT sample remains comparable to conventionally manufactured cast (Ramar et al., 2023) and wrought (Kurdi et al., 2023) counterparts. This suggests that the balance between hardness and stress relief achieved through the 900HT process is still highly favourable.

Simultaneously, when SSP was applied to the 900HT sample, it induced substantial surface compressive residual stresses, with values of −596 ± 7 MPa in the building direction and −636 ± 4 MPa perpendicular to the building direction. These introduced compressive stresses play a pivotal role in enhancing the materials fatigue resistance at the surface. The depth profile analysis unveiled a significant shift towards compressive residual stresses not only on the surface but also within the subsurface after the 900HT+SSP treatment which can be seen from Fig. 6(c–d). These compressive stresses are widely recognized for their ability to enhance resistance to crack propagation as previously reported by Bagherifard and Guagliano (2012), making this treatment combination highly promising for applications that demand exceptional mechanical reliability and durability. High surface roughness has adverse implications for the fatigue strength of materials, impacting their mechanical performance and overall reliability as reported by Nakatani et al. (2019). In this context, the implementation of the SSP has emerged as a promising solution. The SSP method, characterized by its utilization of an Almen intensity of 358 A, played a pivotal role in refining the surface quality of the samples. The process involved the intense interaction of peening media with the sample, effectively levelling the surface. This transformation is notable in Fig. 5(f), where the surface appears significantly smoother and devoid of the previously visible partially melted powder particles. This 900HT+SSP technique has demonstrated its effectiveness in reducing the Ra value from 11.63 μm to 5.04 μm, which represents a reduction of more than 50% of the original roughness.

Furthermore, the 900HT+SSP sample exhibited distinct microstructural changes compared to other conditions, with a notably deeper grain refinement extending approximately 80–90 μm beneath the surface. This unique microstructural transformation is attributed to the dissolution of the cellular microstructure during the 900 °C HT, rendering the material more susceptible to grain deformation during SSP. The presence of these refined grains on both the external surface and within the subsurface of a material can have a profound impact on its mechanical properties, particularly in enhancing its resistance to the initiation of cracks. This effect is primarily attributed to an increase in the stress intensity threshold required for crack nucleation, as reported by Bagherifard et al. (2016) and Kumar et al. (2019). The microhardness analysis of the 900HT+SSP sample underscores the effectiveness of this combination. The initial hardness of the 900HT sample was lower than other conditions but is transformed after SSP. It showcases a remarkable improvement, with a 126% increase in surface hardness, extending the hardness affected depth to a range of 475–525 μm beneath the surface. This significant enhancement is driven by work hardening and grain refinement induced by the SSP process, emphasizing the importance of tailored post-processing techniques.

As for AB+SSP and 600HT+SSP, it is noteworthy that these treatments yielded the same surface compression residual stress levels and hardness as 900HT+SSP. However, when dealing with larger components, the complexity of residual stress fields becomes more pronounced, as highlighted by Ulbricht et al. (2020). In larger samples, tensile residual stresses tend to extend deeper beneath the surface. When SSP is applied to these larger components, it primarily induces compressive residual stresses to a depth of only a few hundred microns, leaving a substantial region beneath the treated surface with retained tensile residual stresses. In such cases, the critical approach involves first alleviating these detrimental tensile residual stresses and then introducing the beneficial compressive residual stresses on the surface and subsurface. This is precisely what the combination of 900HT+SSP achieves, delivering around 90% stress relief while maintaining an appropriate balance. In summary, the integration of the 900HT and SSP processes stands as a key focal point of this study, with results that underscore their combined influence on surface quality, residual stresses, microstructure, and material hardness. The 900HT+SSP combination presents a promising avenue for enhancing material properties and performance, particularly in applications where fatigue and stress corrosion cracking are of paramount importance.

5. Conclusions

This study investigated two distinct stress relief heat treatments combined with severe shot peening when applied to 316 L samples produced via LPBF technology. Conclusively, this work yielded significant insights into the impact of heat treatments and SSP process on the properties of 316 L stainless steel fabricated using LPBF technology. Specifically, the combination of a 900 °C HT followed by SSP has emerged as a promising protocol to address quality-related issues, such as residual stresses and surface finish, potentially leading to improvements in mechanical and stress corrosion cracking performance.

This 900HT+SSP treatment protocol effectively mitigated over 90% of detrimental tensile residual stresses both at the surface and throughout the material's depth followed by induction of beneficial compressive residual stresses on surface. Additionally, 900HT+SSP

significantly reduced surface roughness (Ra) from 11.63 μm to 5.04 μm, and refined the grain structures, all of which are crucial enhancements for improving the mechanical performance of material. Moreover, the dissolution of the cellular microstructure during the 900 °C heat treatment found to have an influence on attaining a distinctive grain deformation depth ranging from 80 μ to 90 μm after SSP. This unique feature could play a pivotal role in delaying crack initiation near the surface and subsurface, thereby contributing to the improved performance of material. The 900 °C heat treatment followed by SSP is further distinguished by a remarkable 126% increase in surface hardness when compared to the base material along with an impressive hardness affected depth of 475–525 μm. This substantial enhancement in surface hardness underscores its potential for superior performance.

The combination of 900 °C HT and SSP offers a balanced material structure with a strong, deformed surface and subsurface, complemented by a softer, coarser-grained interior. This structural configuration is beneficial for minimizing crack initiation on the surface while efficiently arresting cracks within the material. Furthermore, the promise of these findings suggests the need for future investigations into fatigue and stress corrosion cracking tests. The authors intend to investigate and document the fatigue and stress corrosion cracking tests in forthcoming publications.

Funding

This research received financial support from various sources. The Association of Finnish Steel and Metal Producers provided funding with grant number 2139. Additionally, support was received from the European Regional Development Fund (Oulu Region) for "M3D" under grant number A77901 and by Business Finland for the DREAMS project.

CRediT authorship contribution statement

Tejas Gundgire: Conceptualization, Methodology, Investigation, Formal analysis, Visualization, Writing – original draft. **Suvi Santa-aho:** Conceptualization, Writing – review & editing, Supervision. **Timo Rautio:** Conceptualization, Writing – review & editing. **Antti Järvenpää:** Supervision. **Minnamari Vippola:** Conceptualization, Writing – review & editing, Supervision.

Declaration of Competing Interest

The authors declare that they have no known competing financial interests or personal relationships that could have appeared to influence the work reported in this paper.

Data availability

The raw or processed data necessary for replicating these discoveries cannot be disclosed currently, as this data is also integral to an ongoing study.

Acknowledgements

The SEM and EBSD investigations were conducted utilizing the resources and equipment available at Tampere Microscopy Center, located at Tampere University.

References

Attaran, M., 2017. The rise of 3-D printing: the advantages of additive manufacturing over traditional manufacturing. Bus. Horiz. 60, 677–688. https://doi.org/10.1016/j.bushor.2017.05.011.

Bagherifard, S., Guagliano, M., 2012. Fatigue behavior of a low-alloy steel with nanostructured surface obtained by severe shot peening. Eng. Fract. Mech. 81, 56–68. https://doi.org/10.1016/j.engfracmech.2011.06.011.

Bagherifard, S., Slawik, S., Fernández-Pariente, I., Pauly, C., Mücklich, F., Guagliano, M., 2016. Nanoscale surface modification of AISI 316L stainless steel by severe shot peening. Mater. Des. 102, 68–77. https://doi.org/10.1016/j.matdes.2016.03.162.

Bagherifard, S., Beretta, N., Monti, S., Riccio, M., Bandini, M., Guagliano, M., 2018. On the fatigue strength enhancement of additive manufactured AlSi10Mg parts by mechanical and thermal post-processing. Mater. Des. 145, 28–41. https://doi.org/10.1016/j.matdes.2018.02.055.

Bartolomeu, F., Buciumeanu, M., Pinto, E., Alves, N., Carvalho, O., Silva, F.S., Miranda, G., 2017. 316L stainless steel mechanical and tribological behavior—a comparison between selective laser melting, hot pressing and conventional casting. Addit. Manuf. 16, 81–89. https://doi.org/10.1016/j.addma.2017.05.007.

Beretta, S., Romano, S., 2017. A comparison of fatigue strength sensitivity to defects for materials manufactured by AM or traditional processes. Int. J. Fatigue 94, 178–191. https://doi.org/10.1016/j.ijfatigue.2016.06.020.

Bian, P., Shi, J., Shao, X., Du, J., Dai, J., Xu, K., 2018. An Investigation on Residual Stress in 316L Stainless Steel by Selective Laser Melting, in: Volume 1: Additive Manufacturing; Bio and Sustainable Manufacturing. Presented at the ASME 2018 13th International Manufacturing Science and Engineering Conference, American Society of Mechanical Engineers, College Station, Texas, USA, p. V001T01A019. ⟨https://doi.org/10.1115/MSEC2018–6701⟩.

Cabanettes, F., Joubert, A., Chardon, G., Dumas, V., Rech, J., Grosjean, C., Dimkovski, Z., 2018. Topography of as built surfaces generated in metal additive manufacturing: a multi scale analysis from form to roughness. Precis. Eng. 52, 249–265. https://doi.org/10.1016/j.precisioneng.2018.01.002.

Chao, Q., Thomas, S., Birbilis, N., Cizek, P., Hodgson, P.D., Fabijanic, D., 2021. The effect of post-processing heat treatment on the microstructure, residual stress and mechanical properties of selective laser melted 316L stainless steel. Mater. Sci. Eng. A 821, 141611. https://doi.org/10.1016/j.msea.2021.141611.

Dryepondt, S., Nandwana, P., Fernandez-Zelaia, P., List, F., 2021. Microstructure and high temperature tensile properties of 316L fabricated by laser powder-bed fusion. Addit. Manuf. 37, 101723 https://doi.org/10.1016/j.addma.2020.101723.

Dursun, G., Ibekwe, S., Li, G., Mensah, P., Joshi, G., Jerro, D., 2019. Influence of laser processing parameters on the surface characteristics of 316L stainless steel manufactured by selective laser melting. Mater. Today Proc. 26, 387–393. https://doi.org/10.1016/j.matpr.2019.12.061.

Elangeswaran, C., Cutolo, A., Gallas, S., Dinh, T.D., Lammens, N., Erdelyi, H., Schulz, M., Muralidharan, G.K., Thijs, L., Craeghs, T., De Bruycker, E., Boer, K.V., Clijsters, S., Peirs, J., Desmet, W., Van Paepeghem, W., Van Hooreweder, B., 2022. Predicting fatigue life of metal LPBF components by combining a large fatigue database for different sample conditions with novel simulation strategies. Addit. Manuf. 50, 102570 https://doi.org/10.1016/j.addma.2021.102570.

Ford, S., Despeisse, M., 2016. Additive manufacturing and sustainability: an exploratory study of the advantages and challenges. J. Clean. Prod. 137, 1573–1587. https://doi.org/10.1016/j.jclepro.2016.04.150.

Gel'atko, M., Hatala, M., Botko, F., Vandžura, R., Hajnyš, J., Šajgalík, M., Török, J., 2023. Stress Relieving Heat Treatment of 316L Stainless Steel Made by Additive Manufacturing Process. Materials 16, 6461. https://doi.org/10.3390/ma16196461.

Greitemeier, D., Dalle Donne, C., Syassen, F., Eufinger, J., Melz, T., 2016. Effect of surface roughness on fatigue performance of additive manufactured Ti–6Al–4V. Mater. Sci. Technol. 32, 629–634. https://doi.org/10.1179/1743284715Y.0000000053.

Gundgire, T., Jokiaho, T., Santa-aho, S., Rautio, T., Järvenpää, A., Vippola, M., 2022. Comparative study of additively manufactured and reference 316 L stainless steel samples – effect of severe shot peening on microstructure and residual stresses. Mater. Charact. 191, 112162 https://doi.org/10.1016/j.matchar.2022.112162.

Hamada, A., Jaskari, M., Gundgire, T., Järvenpää, A., 2023. Enhancement and underlying fatigue mechanisms of laser powder bed fusion additive-manufactured 316L stainless steel. Mater. Sci. Eng. A 873, 145021. https://doi.org/10.1016/j.msea.2023.145021.

Kamariah, M.S.I.N., Harun, W.S.W., Khalil, N.Z., Ahmad, F., Ismail, M.H., Sharif, S., 2017. Effect of heat treatment on mechanical properties and microstructure of selective laser melting 316L stainless steel. IOP Conf. Ser. Mater. Sci. Eng. 257 https://doi.org/10.1088/1757-899X/257/1/012021.

Kong, D., Ni, X., Dong, C., Zhang, L., Man, C., Yao, J., Xiao, K., Li, X., 2018. Heat treatment effect on the microstructure and corrosion behavior of 316L stainless steel fabricated by selective laser melting for proton exchange membrane fuel cells. Electrochim. Acta 276, 293–303. https://doi.org/10.1016/j.electacta.2018.04.188.

Kruth, J.-P., Yasa, E., Deckers, J., 2008. Roughness improvement in selective laser melting. Proc. 3rd Int. Conf. Polym. Moulds Innov. 170–183.

Kumar, D., Idapalapati, S., Wang, W., Narasimalu, S., 2019. Effect of Surface mechanical treatments on the microstructure-property-performance of engineering alloys. Materials 12, 2503. https://doi.org/10.3390/ma12162503.

Kurdi, A., Tabbakh, T., Basak, A.K., 2023. Microstructural and nanoindentation investigation on the laser powder bed fusion stainless steel 316L. Materials 16, 5933. https://doi.org/10.3390/ma16175933.

Lai, W.-J., Ojha, A., Li, Z., Engler-Pinto, C., Su, X., 2021. Effect of residual stress on fatigue strength of 316L stainless steel produced by laser powder bed fusion process. Prog. Addit. Manuf. 6, 375–383. https://doi.org/10.1007/s40964-021-00164-8.

Li, C., Liu, Z.Y., Fang, X.Y., Guo, Y.B., 2018. Residual stress in metal additive manufacturing. Procedia CIRP 71, 348–353. https://doi.org/10.1016/j.procir.2018.05.039.

Li, R., Liu, J., Shi, Y., Wang, L., Jiang, W., 2012. Balling behavior of stainless steel and nickel powder during selective laser melting process. Int. J. Adv. Manuf. Technol. 59, 1025–1035. https://doi.org/10.1007/s00170-011-3566-1.

Lin, K., Gu, D., Xi, L., Yuan, L., Niu, S., Lv, P., Ge, Q., 2019. Selective laser melting processing of 316L stainless steel: effect of microstructural differences along building

direction on corrosion behavior. Int. J. Adv. Manuf. Technol. 104, 2669–2679. https://doi.org/10.1007/s00170-019-04136-9.
Liu, H., Wei, Y., Tan, C.K.I., Ardi, D.T., Tan, D.C.C., Lee, C.J.J., 2020. XRD and EBSD studies of severe shot peening induced martensite transformation and grain refinements in austenitic stainless steel. Mater. Charact. 168, 110574 https://doi.org/10.1016/j.matchar.2020.110574.
Mercelis, P., Kruth, J.P., 2006. Residual stresses in selective laser sintering and selective laser melting. Rapid Prototyp. J. 12, 254–265. https://doi.org/10.1108/13552540610707013.
Nafar Dastgerdi, J., Jaberi, O., Remes, H., 2022. Influence of internal and surface defects on the fatigue performance of additively manufactured stainless steel 316L. Int. J. Fatigue 163, 107025. https://doi.org/10.1016/j.ijfatigue.2022.107025.
Nakatani, M., Masuo, H., Tanaka, Y., Murakami, Y., 2019. Effect of surface roughness on fatigue strength of Ti-6Al-4V alloy manufactured by additive manufacturing. Procedia Struct. Integr. 19, 294–301. https://doi.org/10.1016/j.prostr.2019.12.032.
Panov, D., Oreshkin, O., Voloskov, B., Petrovskiy, V., Shishkovsky, I., 2022. Pore healing effect of laser polishing and its influence on fatigue properties of 316L stainless steel parts fabricated by laser powder bed fusion. Opt. Laser Technol. 156, 108535 https://doi.org/10.1016/j.optlastec.2022.108535.
Ramar, M., Lakshmanan, M., Kanagasabapathy, M., Shenbaga Velu, P., 2023. Mechanical and tribological properties of SS316L with comparison of SLM and casting methods. Mater. Today Proc., S2214785323013780 https://doi.org/10.1016/j.matpr.2023.03.333.
Rautio, T., Hamada, A., Kumpula, J., Järvenpää, A., Allam, T., 2020. Enhancement of electrical conductivity and corrosion resistance by silver shell-copper core coating of additively manufactured AlSi10Mg alloy. Surf. Coat. Technol. 403, 126426 https://doi.org/10.1016/j.surfcoat.2020.126426.
Rautio, T., Jaskari, M., Gundgire, T., Iso-Junno, T., Vippola, M., Järvenpää, A., 2022. The effect of severe shot peening on fatigue life of laser powder bed fusion manufactured 316L stainless steel. Materials 15, 3517. https://doi.org/10.3390/ma15103517.
Ronneberg, T., Davies, C.M., Hooper, P.A., 2020. Revealing relationships between porosity, microstructure and mechanical properties of laser powder bed fusion 316L stainless steel through heat treatment. Mater. Des. 189, 108481 https://doi.org/10.1016/j.matdes.2020.108481.
Saeidi, K., Gao, X., Zhong, Y., Shen, Z.J., 2015. Hardened austenite steel with columnar sub-grain structure formed by laser melting. Mater. Sci. Eng. A 625, 221–229. https://doi.org/10.1016/j.msea.2014.12.018.
Salman, O.O., Gammer, C., Chaubey, A.K., Eckert, J., Scudino, S., 2019. Effect of heat treatment on microstructure and mechanical properties of 316L steel synthesized by selective laser melting. Mater. Sci. Eng. A 748, 205–212. https://doi.org/10.1016/j.msea.2019.01.110.
Santa-Aho, S., Kiviluoma, M., Jokiaho, T., Gundgire, T., Honkanen, M., Lindgren, M., Vippola, M., 2021. Additive manufactured 316l stainless-steel samples: Microstructure, residual stress and corrosion characteristics after post-processing. Metals 11, 1–16. https://doi.org/10.3390/met11020182.
Saxena, P., Gajera, H., Shah, D., Pancholi, N., 2021. Effect of SLM process parameters on hardness and microstructure of stainless steel 316 material. Mater. Today Proc. https://doi.org/10.1016/j.matpr.2021.09.144.
Sendino, S., Martinez, S., Lartategui, F., Gardon, M., Lamikiz, A., Gonzalez, J.J., 2023. Effect of powder particle size distribution on the surface finish of components manufactured by laser powder bed fusion. Int. J. Adv. Manuf. Technol. 124, 789–799. https://doi.org/10.1007/s00170-022-10423-9.
Shi, W., Wang, P., Liu, Y., Hou, Y., Han, G., 2020. Properties of 316L formed by a 400 W power laser selective laser melting with 250 μm layer thickness. Powder Technol. 360, 151–164. https://doi.org/10.1016/j.powtec.2019.09.059.
Shin, W.-S., Son, B., Song, W., Sohn, H., Jang, H., Kim, Y.-J., Park, C., 2021. Heat treatment effect on the microstructure, mechanical properties, and wear behaviors of stainless steel 316L prepared via selective laser melting. Mater. Sci. Eng. A 806, 140805. https://doi.org/10.1016/j.msea.2021.140805.
Song, R.B., Xiang, J.Y., Hou, D.P., 2011. Characteristics of mechanical properties and microstructure for 316L austenitic stainless steel. J. Iron Steel Res. Int. 18, 53–59. https://doi.org/10.1016/S1006-706X(11)60117-9.
Toribio, J., 1998. Residual stress effects in stress-corrosion cracking. J. Mater. Eng. Perform. 7, 173–182. https://doi.org/10.1361/105994998770347891.
Ulbricht, A., Altenburg, S.J., Sprengel, M., Sommer, K., Mohr, G., Fritsch, T., Mishurova, T., Serrano-Munoz, I., Evans, A., Hofmann, M., Bruno, G., 2020. Separation of the formation mechanisms of residual stresses in LPBF 316L. Metals 10, 1234. https://doi.org/10.3390/met10091234.
Wang, Y.M., Voisin, T., McKeown, J.T., Ye, J., Calta, N.P., Li, Z., Zeng, Z., Zhang, Y., Chen, W., Roehling, T.T., Ott, R.T., Santala, M.K., Depond, P.J., Matthews, M.J., Hamza, A.V., Zhu, T., 2018. Additively manufactured hierarchical stainless steels with high strength and ductility. Nat. Mater. 17, 63–71. https://doi.org/10.1038/nmat5021.
Yadollahi, A., Shamsaei, N., 2017. Additive manufacturing of fatigue resistant materials: challenges and opportunities. Int. J. Fatigue 98, 14–31. https://doi.org/10.1016/j.ijfatigue.2017.01.001.
Yadroitsev, I., Yadroitsava, I., 2015. Evaluation of residual stress in stainless steel 316L and Ti6Al4V samples produced by selective laser melting. Virtual Phys. Prototyp. 10, 67–76. https://doi.org/10.1080/17452759.2015.1026045.
Yin, H., Song, M., Deng, P., Li, L., Prorok, B.C., Lou, X., 2021. Thermal stability and microstructural evolution of additively manufactured 316L stainless steel by laser powder bed fusion at 500–800 ℃. Addit. Manuf. 41, 101981 https://doi.org/10.1016/j.addma.2021.101981.
Zhan, K., Jiang, C.H., Ji, V., 2012. Effect of prestress state on surface layer characteristic of S30432 austenitic stainless steel in shot peening process. Mater. Des. 42, 89–93. https://doi.org/10.1016/j.matdes.2012.05.053.
Zhang, H., Li, C., Yao, G., Shi, Y., Zhang, Y., 2022. Effect of annealing treatment on microstructure evolution and deformation behavior of 304 L stainless steel made by laser powder bed fusion. Int. J. Plast. 155, 103335 https://doi.org/10.1016/j.ijplas.2022.103335.